

EVALUATING EXPLAINABLE AI METHODS IN DEEP LEARNING MODELS FOR EARLY DETECTION OF CEREBRAL PALSY

Kimji N. Pellano¹, Inga Strømke², Daniel Groos¹, Lars Adde³, Espen Alexander F. Ihlen¹

¹ Department of Neuromedicine and Movement Science, Faculty of Medicine and Health Sciences, Norwegian University of Science and Technology, 7034 Trondheim, Norway

² Department of Computer Science, Faculty of Information Technology and Electrical Engineering, Norwegian University of Science and Technology, 7034 Trondheim, Norway

³ Department of Clinical and Molecular Medicine, Faculty of Medicine and Health Sciences, Norwegian University of Science and Technology, 7034 Trondheim, Norway

ABSTRACT

Early detection of Cerebral Palsy (CP) is crucial for effective intervention and monitoring. This paper tests the reliability and applicability of Explainable AI (XAI) methods using a deep learning method that predicts CP by analyzing skeletal data extracted from video recordings of infant movements. Specifically, we use XAI evaluation metrics — namely faithfulness and stability — to quantitatively assess the reliability of Class Activation Mapping (CAM) and Gradient-weighted Class Activation Mapping (Grad-CAM) in this specific medical application. We utilize a unique dataset of infant movements and apply skeleton data perturbations without distorting the original dynamics of the infant movements. Our CP prediction model utilizes an ensemble approach, so we evaluate the XAI metrics performances for both the overall ensemble and the individual models. Our findings indicate that both XAI methods effectively identify key body points influencing CP predictions and that the explanations are robust against minor data perturbations. Grad-CAM significantly outperforms CAM in the RISv metric, which measures stability in terms of velocity. In contrast, CAM performs better in the RISb metric, which relates to bone stability, and the RRS metric, which assesses internal representation robustness. Individual models within the ensemble show varied results, and neither CAM nor Grad-CAM consistently outperform the other, with the ensemble approach providing a representation of outcomes from its constituent models. Both CAM and Grad-CAM also perform significantly better than random attribution, supporting the robustness of these XAI methods. Our work demonstrates that XAI methods can offer reliable and stable explanations for CP prediction models. Future studies should further investigate how the explanations can enhance our understanding of specific movement patterns characterizing healthy and pathological development.

Index Terms— explainable AI, CAM, Grad-CAM, skeleton data, Cerebral Palsy

1. INTRODUCTION

Cerebral Palsy (CP) is the most common motor disability in children, and it is essential to detect it early for effective early intervention and surveillance [1]. Machine learning based technologies are increasingly being explored in the early detection of CP due to its potential for more accurate, accessible, and timely diagnoses. Specifically, deep learning methods have shown great potential in medical diagnostics due to their ability to detect complex patterns in large sets of data. For instance, McCay et al. developed a deep learning framework that classifies infant movements from RGB videos using extracted pose-based features to identify Fidgety Movements (FMs) [2]. Similarly, Groos et al. introduced a method leveraging deep learning to predict CP from skeletal data captured in spontaneous infant movements, validated across a multi-center cohort [3]. Additionally, Zhang et al. designed CP-AGCN, a graph convolutional network (GCN) that uses skeletal data from RGB videos and a frequency-binning module to classify CP risks in infants [4]. Gao et al. implemented a deep learning model to automate early CP detection by analyzing FMs in video sequences [5]. There are several data modalities that can be analyzed for early CP prediction such as in the sensor fusion approach proposed by Kulvicius et al. [6], but this paper focuses on analyzing skeletal data extracted from video recordings via pose estimation, noting its broader applicability to areas such as abnormal gait detection [7], Parkinson’s disease gait assessment [8], fall detection [9], and other health-related applications.

Despite its promising potential, the use of AI in medical diagnostics introduces new challenges, including the widely discussed problem of explainability and transparency. Deep learning models’ inherent lack of interpretability – commonly referred to as the ‘black box’ challenge – is problematic in a medical setting, where clear explanations for diagnoses is a requirement. To build trust in AI-driven diagnostic tools among clinicians and patients, and facilitate possible imple-

mentation in clinical use, it is crucial to understand the predictions made by these tools. This need for transparency and trust aligns with the requirements of the EU’s recently implemented AI regulation, the AI Act, which classifies applications that could affect the life, safety, and health of people as high-risk [10], and thereby requires these applications to provide explanations before they are allowed for deployment.

Prechtl’s General Movements Assessment (GMA) is a highly reliable diagnostic tool for early detection of CP and is based upon medical experts observing normal versus abnormal movement patterns [11], yet it faces several challenges. These include the requirement for training the clinicians performing GMA to achieve proficiency in assessment techniques, the subjective nature of visual analysis which can lead to variability in interpretations, the time-intensive process of manually analyzing movements, and long-term costs associated with training and qualifying medical experts [12]. Using AI can potentially address these issues by automating the detection process of abnormal movement patterns, thereby reducing the burden on the limited number of trained GMA experts, while providing objective and consistent analysis, and significantly reducing the time needed for assessments. However, it is crucial that this does not compromise the interpretability that clinicians value in Prechtl’s GMA, ensuring that the insights offered by AI systems are sufficiently explained and thus complementary and understandable from a clinician’s perspective.

To aid healthcare providers in understanding AI diagnoses, Explainable AI (XAI) methods can be used. For instance, in medical imaging, XAI has facilitated cancer detection [13]. In the CP prediction space, Sakkos et al. introduced a deep learning framework using RGB videos, with visualization showing segmented body parts with movement abnormalities and their contribution to the classification result [14]. Reflecting on the boom of automated solutions for Prechtl’s GMA and the growing trend of incorporating XAI in diverse medical applications, and in anticipation of the legal requirements when deploying AI-assisted medical diagnostic tools, our study aims to bridge a crucial gap: despite the evident progress, the application of XAI in skeleton-based CP diagnosis remains understudied. To assess the trustworthiness of the explanations generated by these methods, we advocate for the use of metrics that objectively evaluate the reliability of the explanations. This is crucial because AI-based analysis of skeletal data could extend to several other previously mentioned high-stakes applications, beyond CP prediction. However, the application of domain-specific knowledge across such a broad spectrum of potential uses could become cumbersome. Therefore, we also suggest adopting the metrics evaluated in this study as foundational benchmarks for assessing XAI techniques, and then supplementing them with specialized domain knowledge to enhance and confirm their validity further.

This study explores the applicability of Class Activation

Mapping (CAM) and Gradient-Weighted Class Activation Mapping (Grad-CAM), which are widely used XAI methods in Convolutional Neural Network (CNN) models, to Graph Convolutional Network (GCN)-based models for Cerebral Palsy (CP) prediction. Specifically, we investigate whether these XAI methods can effectively differentiate between important and unimportant body points influencing CP predictions. Additionally, we assess the stability of explanations when the input data undergo minor perturbations.

The contributions of our study are:

- An objective evaluation framework to assess the reliability of different XAI methods used in a specific medical application, which is skeleton-based early detection of CP from infants’ spontaneous movements.
- The comparative analysis of different XAI methods (CAM and Grad-CAM), providing insight into their effectiveness in the context of early CP detection, which can potentially be used in other high-stakes applications.
- Showing the possible use of XAI methods to guide further research in early CP diagnosis. For example, it can potentially be used to discover specific infant movement patterns that are correlated with later CP status that might be complementary information for GMA experts focusing on gestalt infant movements. The evaluation of these XAI methods for this specific application is the first step towards determining the most reliable explanations that can provide valuable insights into specific infant movements.
- The application of XAI evaluation metrics to an ensemble of models for CP prediction, providing insight into the collective robustness of the aggregated ensemble and individual model explanations against minor perturbations.

1.1. XAI Methods

The following section discusses the various XAI methods implemented for the skeleton-based CP prediction model. These methods will subsequently be assessed using the XAI evaluation metrics.

1.1.1. Class Activation Mapping (CAM)

CAM was originally introduced as a method for identifying important pixels in an image [15] as determined by a CNN model. It projects the model’s output layer weights onto a convolutional layer’s feature maps (usually from the final layer), creating a heatmap that highlights the areas influencing the network’s predictions,

$$e_{X, \text{CAM}} = \sum_n w_n^{\text{class}} F^n . \quad (1)$$

CAM can be generalized and applied to other convolution-based models if the weights after Global Average Pooling (GAP) for a specific *class* and the n th feature map F^n are multiplied, as shown in Equation (1). For example, in human activity recognition (HAR) using 3D skeleton graphs as input to a GCN, important body points in the skeleton data can be highlighted, as shown by Song et al. with their work on EfficientGCN [16].

1.1.2. Gradient-Weighted Class Activation Mapping (Grad-CAM)

CAM has several weaknesses, such as the lack of flexibility in model architecture due to the need for a GAP layer and a Fully Connected (FC) layer for classification. Gradient-weighted Class Activation Mapping (Grad-CAM) [17] addresses this by using gradients entering the FC layer instead of weights, calculated via

$$e_{X, \text{Grad-CAM}} = \sum_n \alpha_n^{\text{class}} F^n, \quad (2)$$

thus making it adaptable to various CNN architectures. Since the introduction of Grad-CAM, many other CAM-based methods have been introduced to further improve the original CAM. Similarly to CAM, Grad-CAM has been shown to be applicable to GCN-based HAR using skeleton data, as illustrated by Das et al. [18].

1.2. XAI Evaluation Metrics

In our previous work [19], we explored various metrics proposed in [20] to evaluate explanations from different XAI methods within the context of skeleton-based HAR. Building on these foundations, this paper aims to extend these evaluation techniques to a specific medical application, which is skeleton-based CP prediction. The following subsections give a brief overview of the applied metrics, illustrating their applicability and relevance in a specific medical use-case. Consider X as the original input data, with its corresponding explanation e_X , and let $f(\cdot)$ denote the model's output, representing CP risk. Then, X' is the perturbed version of X , and $e_{X'}$ stands for its corresponding explanation following the perturbation. Top- k refers to the most important features in the input data, while non-top- k refers to the remaining, less important features.

1.2.1. Faithfulness

Fidelity or faithfulness [21, 22, 23] checks whether an explanation accurately identifies the features that influence a model's predictions. The Prediction Gap on Important features (PGI) in Equation (3) quantifies the prediction change when key features are altered, while the Prediction Gap on Unimportant features (PGU) in Equation (4) measures the

change when minor features are modified. Ideally, when important features are perturbed, there should be a significant change in the model prediction. Conversely, perturbing unimportant features should have little effect on the prediction. By this logic, a good XAI method should identify both important and unimportant features in a way that results in a high PGI and a low PGU.

$$PGI(X, f, e_X, k) = \mathbb{E}_{X' \sim \text{perturb}(X, e_X, \text{top-}k)} [|f(X) - f(X')|] \quad (3)$$

$$PGU(X, f, e_X, k) = \mathbb{E}_{X' \sim \text{perturb}(X, e_X, \text{non top-}k)} [|f(X) - f(X')|] \quad (4)$$

1.2.2. Stability

Stability or robustness [24, 25], measures how much an explanation changes relative to changes in the model's input, output, or internal representation when the original input data undergo minor perturbations, as shown in Equations (5)–(7). Relative Input Stability (RIS) includes three components for each of the model's multiple input streams: position, velocity, and bone, referred to as RISp, RISv, and RISb, respectively. ROS refers to Relative Output Stability and RRS refers to Relative Representation Stability. To better understand these concepts in relation to the variables in the model, please refer to Fig. 1a, which illustrates the main architecture of the network. \mathcal{L}_X in Equation (7) denotes the model's internal representation, which in our study is the logits from the layer preceding the softmax activation function. A stability score of zero is ideal, as it means that visually imperceptible perturbations do not change the explanation at all.

$$\text{RIS}(X, X', e_X, e_{X'}) = \max_{X'} \frac{\left\| \frac{(e_X - e_{X'})}{e_X} \right\|_p}{\max \left(\left\| \frac{(X - X')}{X} \right\|_p, \epsilon_{\min} \right)}, \quad (5)$$

$\forall X' \text{ s.t. } X' \in \mathcal{N}_X; f(X) = f(X')$

$$\text{ROS}(X, X', e_X, e_{X'}) = \max_{X'} \frac{\left\| \frac{(e_X - e_{X'})}{e_X} \right\|_p}{\max \left(\left\| \frac{(f(X) - f(X'))}{f(X)} \right\|_p, \epsilon_{\min} \right)}, \quad (6)$$

$\forall X' \text{ s.t. } X' \in \mathcal{N}_X; f(X) = f(X')$

$$\text{RRS}(X, X', e_X, e_{X'}) = \max_{X'} \frac{\left\| \frac{(e_X - e_{X'})}{e_X} \right\|_p}{\max \left(\left\| \frac{(\mathcal{L}_X - \mathcal{L}_{X'})}{\mathcal{L}_X} \right\|_p, \epsilon_{\min} \right)}, \quad (7)$$

$\forall X' \text{ s.t. } X' \in \mathcal{N}_X; f(X) = f(X')$

1.3. CP Dataset

The dataset used in this study originates from Groos et al. [3], and is made up of 557 infants at elevated risk of perinatal brain injury, gathered from 13 different hospitals in Norway, Belgium, India, and the US. In compliance with Prechtl’s GMA tool protocols, the infants were filmed during the FM period occurring between 9 and 18 weeks’ corrected age. Using the CP decision tree from the Surveillance of Cerebral Palsy in Europe [26], a pediatrician determined their CP statuses at 12 months corrected age or older. Of the 557 videos, 75% were allocated for model training and validation, while the remaining 25% formed the test set which is used in this paper.

Of the 139 videos in the test set, 21 are true CP cases and 118 are true No CP cases. For the XAI metrics testing, extracted skeleton tracker data from the original videos were used instead of the videos themselves. Given the long testing times for computing XAI metrics (approximately 1 hour per 5-second window on an RTX3090 GPU), random 5-second window samples were taken from the tracker data, proportional to the video length. For example, only one 5-second window sample was taken from the shortest videos.

Moreover, since testing for *stability* metric requires that the true label matches the predicted label, only correctly predicted data were used, resulting in 15 CP and 111 No CP cases. From these, 24 random 5-second windows were selected from CP data and 136 from No CP data, maintaining the original CP to No-CP ratio. Additionally, windows at the beginning or end of the videos were avoided to reduce noise, and non-overlapping 5-second windows were chosen to avoid redundant data.

1.4. CP Prediction Model

The same deep learning-based CP prediction model from the Groos et al. study [3] was evaluated for the XAI metrics. This model uses a GCN architecture to process infants’ biomechanical movement properties, namely positions, velocities, and bones (distances between body keypoints). The GCN architecture was optimized through an automatic search, which created 70 distinct model instances, each trained on different sections of the dataset. Refinement of the model involved hyperparameter tuning and an automatic Neural Architecture Search (NAS) approach, exploring various architectural designs and configurations. The final Ensemble-NAS-GCN model combines predictions from the 70 GCN instances, as illustrated in Fig. 1b, where the model number represents a unique architecture and the portion number denotes the specific training/validation fold used for that model. Details about each of the 10 GCN model architectures can be found in the Appendix Table 3. Each model instance analyzes 5-second windows, with the CP risk determined as the median prediction across the ensemble. Similarly, for each 5-second window, the XAI attribution scores (i.e. CAM or Grad-CAM)

from all 70 GCN instances were collected and unified by calculating the median score for each body point. There were no alterations made to the CP prediction pipeline except for capturing intermediate variables, such as model weights and gradients needed for the XAI metric evaluation.

2. METHODS

2.1. Skeleton Data Perturbation

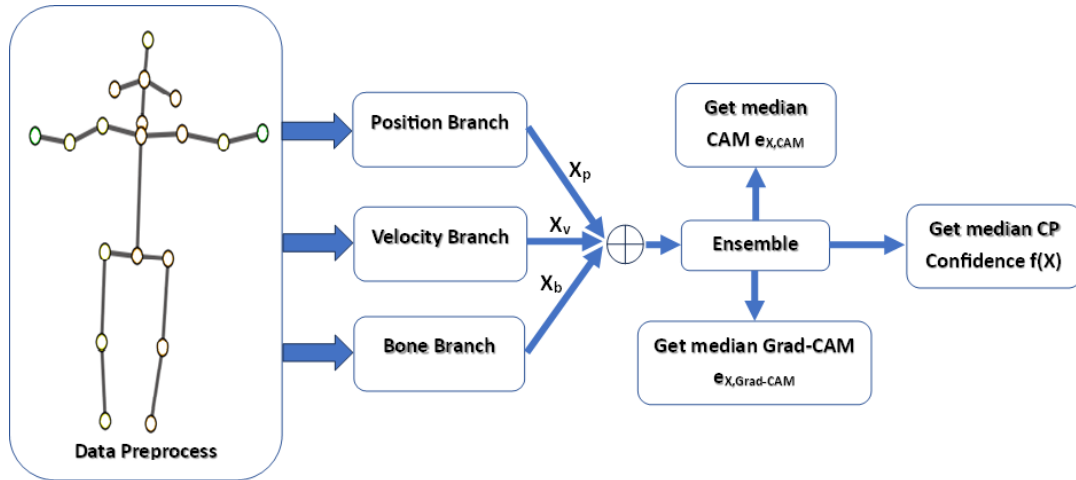
As demonstrated in our previous work [19], skeleton joints can be perturbed by converting Cartesian coordinates to spherical coordinates. This is performed using the equations below, where dx and dy represent the perturbation magnitudes along the x - and y -axes respectively, P is the original point, P' is the new perturbed point, x' and y' are the new coordinates, x and y are the original coordinates, and θ is the randomly generated azimuthal angle:

$$\begin{aligned} r &= \|P - P'\| \\ dx &= r \cos \theta \\ x' &= x + dx \\ dy &= r \sin \theta \\ y' &= y + dy. \end{aligned}$$

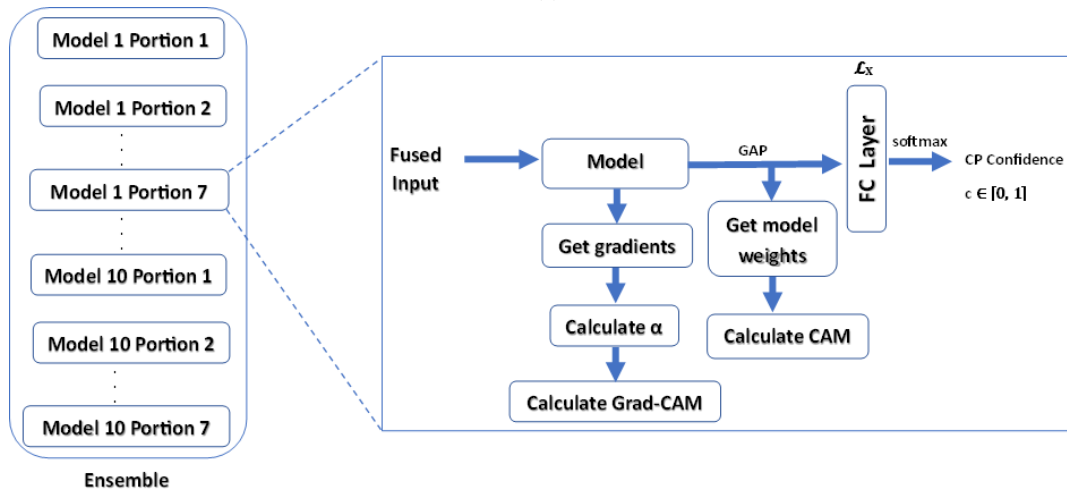
Equations (5), (6), (7) require that the perturbed input data X' remains close to the original data X , which also maintains accurate human kinematics and preserving the integrity of model predictions. To achieve this, r is set to 1% of the median height of the infant across all frames in a 5-second window. The infant coordinate data are in pixels and height is calculated as the Euclidean distance between the head and left ankle. The values dx and dy are computed once for each joint and applied consistently across all video frames, producing a perturbed 2D point.

2.2. Calculation and Evaluation of XAI Metrics

The first step is to obtain the explanation for the original unperturbed data. The skeleton tracker data is fed into the CP prediction pipeline after *Data Preprocess* stage as shown in Fig. 1a. Each model in the ensemble generates its own explanation according to Equations (1) and (2), as shown in Fig. 1b). These individual explanations are combined by calculating the median values, representing the overall explanation for the ensemble. Similarly, individual model output predictions are combined by taking the median value, representing the ensemble’s output prediction. This process yields the terms $f(X)$, e_X , and X . The term \mathcal{L}_X is derived by collecting internal representations from the final FC layer before the softmax function of each model and flattening them into a single array.



(a)



(b)

Fig. 1: Overview of CP prediction ensemble pipeline, showing (a) the variables for XAI metrics evaluation, and (b) the processing steps for each model in the CP prediction ensemble.

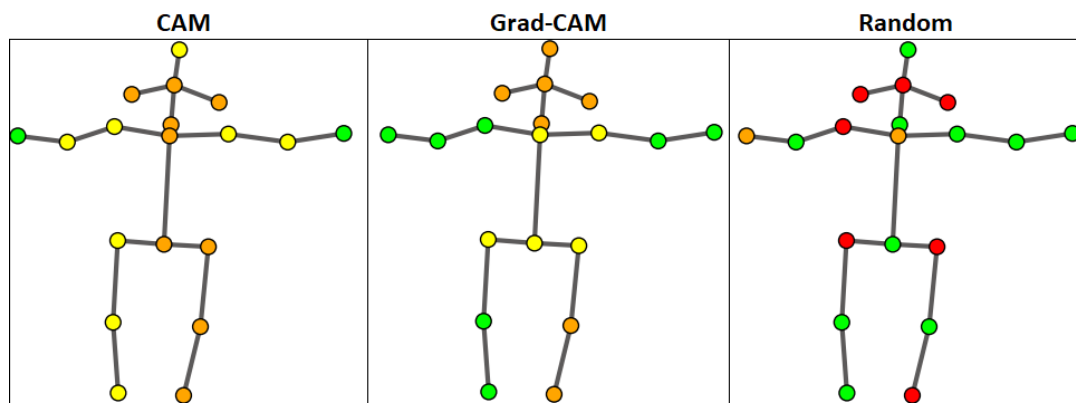


Fig. 2: Sample visualization of attribution scores coming from the ensemble model's XAI methods tested using the same video. From left to right: CAM, Grad-CAM, and random method. Green indicates low attribution scores, yellow indicates moderate scores, orange shows high scores, and red signifies very high scores relative to the defined threshold score.

Next, the body keypoints are ranked by importance from highest to lowest, and the top-k and non top-k joints are identified as determined by the ensemble’s explanations. A sample visualization of these attribution scores, translated into color-coded importance indicators, is shown in Fig. 2, where green indicates low scores, yellow indicates moderate scores, orange indicates high scores, and red indicates very high scores relative to a threshold of 0.3. Perturbed varieties of the original data are generated as outlined in the previous section. Each 5-second window undergoes $n = 50$ perturbations at a specified magnitude r . The top-k body points (where $k = 1$ to 19) are systematically perturbed n times and then fed into the model to calculate PGI, then the remaining points are perturbed to compute PGU. Stability metrics are also computed using the explanations for the n perturbations and the resulting intermediate values in the ensemble. We use the Area Under the Curve (AUC) to combine the calculated metric scores across all k values for each video into a single score. We then compute the mean and standard deviation of these AUCs in all videos to obtain the overall metric values. Since the metrics are unitless, the results are also compared against a random method that assigns feature attribution scores randomly, which represents the worst performance for an XAI method when subjected to a perturbation magnitude r .

To compare the ensemble’s XAI metrics performance with individual models, we conducted the same test on each model architecture. The ensemble consists of 70 model instances across 10 unique architectures, each trained on 7 different folds. Model 9, portion 5 achieved the highest AUC-ROC score in the test set, and thus portion 5 was used to represent each architecture in the tests. The same test pipeline is implemented as described above, except that the intermediate values for the metrics were derived from the individual models rather than the ensemble. Note that each model and the ensemble have unique sets of top-k and non top-k body points identified, resulting in distinct perturbed skeleton data, requiring separate tests. Using our hardware setup with RTX3090 GPU, the calculation for the ensemble took approximately 163 hours for CAM, 238 hours for Grad-CAM, and 120 hours for random method. The calculation for CAM, Grad-CAM, and random methods combined took approximately 24 hours for each model. The results for the individual models can be found in the Appendix Tables 1 and 2. Lastly, we conducted an unpaired t-test to determine the statistical significance of the differences in metric results between CAM and Grad-CAM. For completeness, we also performed t-tests comparing CAM versus random attribution and Grad-CAM versus random attribution, expecting significant statistical differences in both tests.

3. RESULTS AND DISCUSSION

A line plot is used to comparatively show the metrics performance of each XAI method in Fig. 3, which shows the relative performances for each metric based on their positions on the horizontal axis. The exact numerical results with confidence intervals are shown in the Appendix Tables 1 and 2.

3.1. Faithfulness

PGI results indicate that the ensemble’s predictions are influenced by key features identified by the two XAI methods (i.e. the change in output probability $f(X)$ increases when important nodes are perturbed), with a significant difference compared to the random attribution at $p < 0.005$ for both CAM versus random and Grad-CAM versus random. There was no significant difference in PGI and PGU between CAM and Grad-CAM. Overall, the faithfulness tests indicate that XAI methods effectively distinguish important from unimportant body points influencing predictions.

3.2. Stability

The plots of RISp, RISv, RISb, ROS, and RRS in Fig. 3 immediately show us that random explanations cause significant changes in the stability results, with $p < 0.005$ for both CAM versus random and Grad-CAM versus random. This indicates that both XAI methods are less susceptible to large explanation changes with small input perturbations. Most notably, Grad-CAM offers a highly significant improvement (with $p < 8.507 \times 10^{-7}$) of input stability compared to CAM for RISv of the ensemble model. In contrast, CAM offers a significantly better input stability (with $p < 0.05$) compared to Grad-CAM for RISb and RRS. The result for the stability and faithfulness metric for the different GCN models in ensemble can be found in the Appendix Tables 1 and 2.

4. CONCLUSION AND RECOMMENDATION

This study evaluated the reliability and robustness of two XAI techniques, CAM and Grad-CAM, within a deep learning ensemble model. The faithfulness metrics show both methods are effective in identifying important and unimportant body points influencing CP predictions, while stability tests demonstrate robustness against minor data perturbations. Specifically, CAM significantly outperformed Grad-CAM in RISb and RRS, while Grad-CAM excelled in RISv. The choice of XAI method depends on the specific application and key metrics. For instance, to identify potential movement biomarkers for CP related to joint velocity, Grad-CAM is recommended for its superior RISv performance. This also suggests exploring the velocity input branch for possible CP movement biomarkers, which aligns with previous studies [27, 28, 29, 30] where a velocity parameter is used in classical

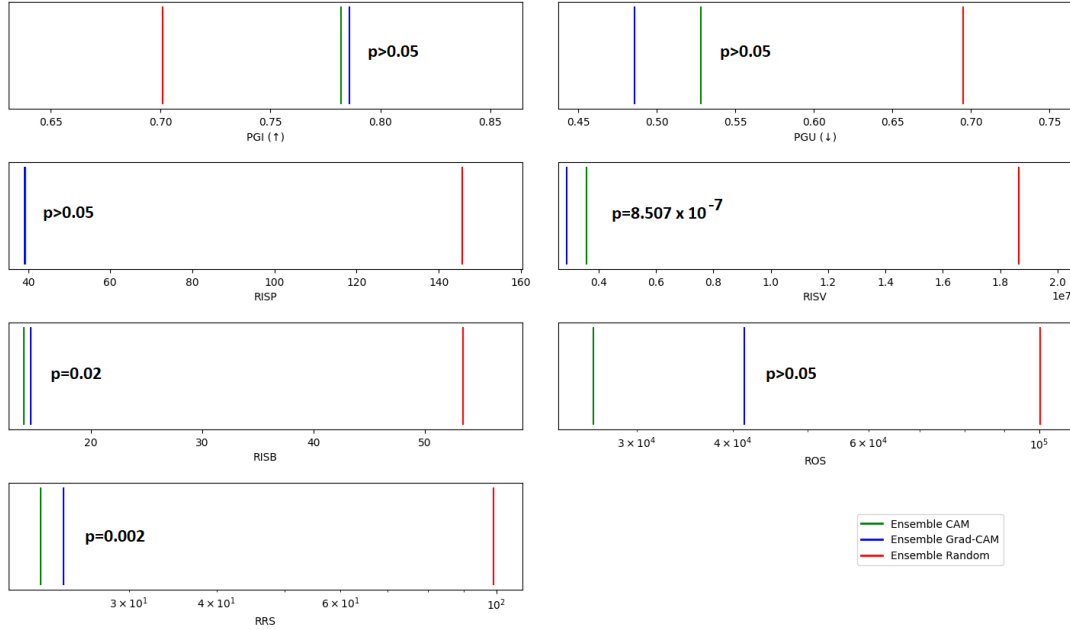


Fig. 3: A line plot showing the metrics test results. PGI (↑) indicates that higher scores denote better performance, while PGU (↓) indicates that lower scores denote better performance. For stability metrics (RISP, RISV, RISB, ROS, RRS), values closer to zero are optimal. ROS and RRS are plotted on logarithmic scales to better display a wide range of values. Each plot also shows the p-value from the unpaired t-test between CAM and Grad-CAM for easier reference on the statistical significance of their difference.

machine learning assessments of CP. If similar explanations for body points are found in multiple 5-second windows, Grad-CAM offers better insight into body point velocity due to its stable explanations despite input variations. Conversely, for quick explanations (i.e. for visual inspection purposes), CAM is preferable due to its faster calculation time.

Individual models in the ensemble show varied results in metrics tests, while the ensemble provides a combined outcome from its constituent models. In our previous work [19], we applied metrics tests to a single GCN-based model, limiting generalizability. This study has evaluated XAI metrics in both an ensemble and the individual models composing it, revealing that neither CAM nor Grad-CAM consistently outperforms the other in all metrics. Overall, our findings demonstrate that both XAI methods can provide reliable and stable explanations in CP prediction models. By finding patterns and doing further studies into the explanations, these could potentially supplement GMA observers with specialized domain knowledge, contributing to more interpretable and trustworthy AI diagnostics. The study’s insights into the comparative performance of CAM and Grad-CAM can also guide future research in improving AI explainability in other high-stakes medical applications. As a next step, it is crucial to introduce more XAI metrics that incorporate domain-specific knowledge to further validate the relevance and accuracy of the explanations provided. It is also necessary to per-

form clinical interpretations on the explanations to enhance the practical utility of the models.

5. REFERENCES

- [1] I. Novak, C. Morgan, L. Adde, J. Blackman, R. N. Boyd, J. Brunstrom-Hernandez, G. Cioni, D. Damiano, J. Darrah, A.-C. Eliasson, and et al., “Early, accurate diagnosis and early intervention in cerebral palsy: advances in diagnosis and treatment,” *JAMA Pediatrics*, vol. 171, no. 9, pp. 897–907, 2017.
- [2] K. D. McCay, E. S. Ho, H. P. Shum, G. Fehringer, C. Marcroft, and N. D. Embleton, “Abnormal infant movements classification with deep learning on pose-based features,” *IEEE Access*, vol. 8, pp. 51 582–51 592, 2020.
- [3] D. Groos, L. Adde, S. Aubert, L. Boswell, R. A. De Regnier, T. Fjørtoft, D. Gaebler-Spira, A. Haukeland, M. Loenneken, M. Msall, and et al., “Development and validation of a deep learning method to predict cerebral palsy from spontaneous movements in infants at high risk,” *JAMA Network Open*, vol. 5, no. 7, pp. e2 221 325–e2 221 325, 2022.
- [4] H. Zhang, E. S. Ho, and H. P. Shum, “Cp-agcn: Pytorch-based attention informed graph convolutional network

- for identifying infants at risk of cerebral palsy,” *Software Impacts*, vol. 14, p. 100419, 2022.
- [5] Q. Gao, S. Yao, Y. Tian, C. Zhang, T. Zhao, D. Wu, G. Yu, and H. Lu, “Automating general movements assessment with quantitative deep learning to facilitate early screening of cerebral palsy,” *Nature Communications*, vol. 14, no. 1, p. 8294, 2023.
- [6] T. Kulvicius, D. Zhang, L. Poustka, S. Bölte, L. Jahn, S. Flügge, M. Kraft, M. Zweckstetter, K. Nielsen-Saines, and F. Wörgötter, “Deep learning empowered sensor fusion to improve infant movement classification,” *arXiv preprint arXiv:2406.09014*, 2024.
- [7] T.-N. Nguyen, H.-H. Huynh, and J. Meunier, “Skeleton-based abnormal gait detection,” *Sensors*, vol. 16, no. 11, p. 1792, 2016.
- [8] J. Ajay, C. Song, A. Wang, J. Langan, Z. Li, and W. Xu, “A pervasive and sensor-free deep learning system for parkinsonian gait analysis,” in *2018 IEEE EMBS International Conference on Biomedical & Health Informatics (BHI)*, 2018, pp. 108–111.
- [9] W. Chen, Z. Jiang, H. Guo, and X. Ni, “Fall detection based on key points of human-skeleton using openpose,” *Symmetry*, vol. 12, no. 5, p. 744, 2020.
- [10] European Commission. (2024, aug) Ai act enters into force. Accessed: Aug. 7, 2024. [Online]. Available: <https://commission.europa.eu/news/ai-act-enters-force-2024-08-01>
- [11] E. Ricci, C. Einspieler, and A. K. Craig, “Feasibility of using the general movements assessment of infants in the united states,” *Physical & Occupational Therapy in Pediatrics*, vol. 38, no. 3, pp. 269–279, 2018.
- [12] N. Silva, D. Zhang, T. Kulvicius, A. Gail, C. Barreiros, S. Lindstaedt, M. Kraft, S. Bölte, L. Poustka, K. Nielsen-Saines, and et al., “The future of general movement assessment: The role of computer vision and machine learning—a scoping review,” *Research in Developmental Disabilities*, vol. 110, p. 103854, 2021.
- [13] M. A. Gulum, C. M. Trombley, and M. Kantardzic, “A review of explainable deep learning cancer detection models in medical imaging,” *Applied Sciences*, vol. 11, no. 10, p. 4573, 2021.
- [14] D. Sakkos, K. D. McCay, C. Marcroft, N. D. Embleton, S. Chattopadhyay, and E. S. Ho, “Identification of abnormal movements in infants: A deep neural network for body part-based prediction of cerebral palsy,” *IEEE Access*, vol. 9, pp. 94 281–94 292, 2021.
- [15] B. Zhou, A. Khosla, A. Lapedriza, A. Oliva, and A. Torralba, “Learning deep features for discriminative localization,” in *Proceedings of the IEEE Conference on Computer Vision and Pattern Recognition*, 2016, pp. 2921–2929.
- [16] Y.-F. Song, Z. Zhang, C. Shan, and L. Wang, “Constructing stronger and faster baselines for skeleton-based action recognition,” *IEEE Transactions on Pattern Analysis and Machine Intelligence*, vol. 45, no. 2, pp. 1474–1488, 2022.
- [17] R. R. Selvaraju, M. Cogswell, A. Das, R. Vedantam, D. Parikh, and D. Batra, “Grad-cam: Visual explanations from deep networks via gradient-based localization,” in *Proceedings of the IEEE International Conference on Computer Vision*, 2017, pp. 618–626.
- [18] P. Das and A. Ortega, “Gradient-weighted class activation mapping for spatio temporal graph convolutional network,” in *ICASSP 2022-2022 IEEE International Conference on Acoustics, Speech and Signal Processing (ICASSP)*, 2022, pp. 4043–4047.
- [19] K. N. Pellano, I. Strümke, and E. A. F. Ihlen, “From movements to metrics: Evaluating explainable ai methods in skeleton-based human activity recognition,” *Sensors*, vol. 24, no. 6, p. 1940, 2024.
- [20] C. Agarwal, S. Krishna, E. Saxena, M. Pawelczyk, N. Johnson, I. Puri, M. Zitnik, and H. Lakkaraju, “Openxai: Towards a transparent evaluation of model explanations,” *Advances in Neural Information Processing Systems*, vol. 35, pp. 15 784–15 799, 2022.
- [21] D. Alvarez Melis and T. Jaakkola, “Towards robust interpretability with self-explaining neural networks,” *Advances in Neural Information Processing Systems*, vol. 31, 2018.
- [22] J. Zhou, A. H. Gandomi, F. Chen, and A. Holzinger, “Evaluating the quality of machine learning explanations: A survey on methods and metrics,” *Electronics*, vol. 10, no. 5, p. 593, 2021.
- [23] A. F. Markus, J. A. Kors, and P. R. Rijnbeek, “The role of explainability in creating trustworthy artificial intelligence for health care: a comprehensive survey of the terminology, design choices, and evaluation strategies,” *Journal of Biomedical Informatics*, vol. 113, p. 103655, 2021.
- [24] D. Alvarez-Melis and T. S. Jaakkola, “On the robustness of interpretability methods,” *arXiv preprint arXiv:1806.08049*, 2018.

- [25] C. Agarwal, N. Johnson, M. Pawelczyk, S. Krishna, E. Saxena, M. Zitnik, and H. Lakkaraju, "Rethinking stability for attribution-based explanations," *arXiv preprint arXiv:2203.06877*, 2022.
- [26] C. Cans, "Surveillance of cerebral palsy in europe: a collaboration of cerebral palsy surveys and registers," *Developmental Medicine & Child Neurology*, vol. 42, no. 12, pp. 816–824, 2000.
- [27] L. Meinecke, N. Breitbach-Faller, C. Bartz, R. Damen, G. Rau, and C. Disselhorst-Klug, "Movement analysis in the early detection of newborns at risk for developing spasticity due to infantile cerebral palsy," *Human Movement Science*, vol. 25, no. 2, pp. 125–144, 2006.
- [28] L. Adde, J. L. Helbostad, A. R. Jensenius, G. Taraldsen, and R. Støen, "Using computer-based video analysis in the study of fidgety movements," *Early Human Development*, vol. 85, no. 9, pp. 541–547, 2009.
- [29] L. Adde, J. L. Helbostad, A. R. Jensenius, G. Taraldsen, K. H. Grunewaldt, and R. Støen, "Early prediction of cerebral palsy by computer-based video analysis of general movements: a feasibility study," *Developmental Medicine & Child Neurology*, vol. 52, no. 8, pp. 773–778, 2010.
- [30] A. Stahl, C. Schellewald, O. Stavadahl, O. M. Aamo, L. Adde, and H. Kirkerod, "An optical flow-based method to predict infantile cerebral palsy," *IEEE Transactions on Neural Systems and Rehabilitation Engineering*, vol. 20, no. 4, pp. 605–614, 2012.

Table 1: Metrics Test Results for Ensemble and Individual Models (part 1)

PGI	CAM	Grad-CAM	Random
Ensemble	0.782 ± 0.141	0.786 ± 0.137	0.701 ± 0.130
Model 1	1.086 ± 0.175	1.088 ± 0.174	0.971 ± 0.149
Model 2	1.379 ± 0.264	1.359 ± 0.263	1.132 ± 0.234
Model 3	1.305 ± 0.295	1.303 ± 0.296	1.179 ± 0.280
Model 4	1.085 ± 0.244	0.976 ± 0.211	0.909 ± 0.199
Model 5	1.516 ± 0.315	1.535 ± 0.315	1.234 ± 0.284
Model 6	1.231 ± 0.218	1.247 ± 0.222	1.146 ± 0.200
Model 7	0.711 ± 0.216	0.739 ± 0.209	0.623 ± 0.168
Model 8	1.523 ± 0.181	1.521 ± 0.181	1.378 ± 0.157
Model 9	1.048 ± 0.193	1.333 ± 0.253	1.053 ± 0.196
Model 10	0.680 ± 0.224	0.621 ± 0.208	0.762 ± 0.283
PGU	CAM	Grad-CAM	Random
Ensemble	0.528 ± 0.095	0.486 ± 0.103	0.695 ± 0.128
Model 1	0.818 ± 0.152	0.817 ± 0.152	1.063 ± 0.172
Model 2	0.686 ± 0.138	0.683 ± 0.138	0.918 ± 0.182
Model 3	0.946 ± 0.242	0.939 ± 0.242	1.162 ± 0.279
Model 4	0.543 ± 0.105	0.633 ± 0.130	0.885 ± 0.184
Model 5	0.676 ± 0.150	0.680 ± 0.150	1.066 ± 0.197
Model 6	0.990 ± 0.179	0.990 ± 0.179	1.032 ± 0.200
Model 7	0.613 ± 0.175	0.534 ± 0.146	0.624 ± 0.172
Model 8	1.170 ± 0.154	1.169 ± 0.154	1.339 ± 0.165
Model 9	1.028 ± 0.218	0.754 ± 0.148	0.981 ± 0.188
Model 10	0.525 ± 0.173	0.628 ± 0.209	0.588 ± 0.178
RISp	CAM	Grad-CAM	Random
Ensemble	39.328 ± 3.257	39.167 ± 2.544	145.805 ± 4.371
Model 1	48.779 ± 3.083	48.779 ± 3.083	162.523 ± 4.652
Model 2	37.047 ± 2.456	37.055 ± 2.458	162.542 ± 5.308
Model 3	40.152 ± 2.474	39.874 ± 2.457	161.785 ± 4.371
Model 4	33.725 ± 1.730	34.488 ± 3.546	161.706 ± 4.784
Model 5	30.154 ± 2.790	30.154 ± 2.790	162.705 ± 4.718
Model 6	37.997 ± 4.055	38.262 ± 4.056	162.625 ± 5.045
Model 7	36.014 ± 2.067	37.290 ± 3.642	165.739 ± 4.367
Model 8	49.747 ± 2.182	49.751 ± 2.181	157.211 ± 5.326
Model 9	37.048 ± 2.160	26.384 ± 3.928	162.735 ± 4.865
Model 10	35.644 ± 3.336	53.884 ± 3.070	160.971 ± 5.069
RISv	CAM	Grad-CAM	Random
Ensemble	3585402.774 ± 544958.663	2888248.714 ± 486164.011	18641327.196 ± 3924550.555
Model 1	5013896.473 ± 733566.854	5013897.457 ± 733567.024	22808539.350 ± 6802897.522
Model 2	3826587.193 ± 1326590.444	3842761.467 ± 1328900.588	22426153.524 ± 4301241.358
Model 3	3025573.782 ± 581141.137	3021450.227 ± 581182.591	21338036.160 ± 5862771.374
Model 4	3756392.648 ± 438413.881	3566904.056 ± 719258.913	21367999.081 ± 4543133.766
Model 5	2271316.786 ± 577805.929	2271316.654 ± 577805.925	22637633.435 ± 4817636.850
Model 6	5008019.480 ± 868948.611	5098120.204 ± 882587.754	22424391.642 ± 5949317.869
Model 7	4669245.654 ± 571611.191	4169000.548 ± 1686004.537	23354361.639 ± 5345484.607
Model 8	5592108.186 ± 760098.099	5586872.125 ± 760912.793	19221557.170 ± 3435013.322
Model 9	5011561.220 ± 1588484.050	2193192.993 ± 951410.356	22146716.652 ± 6454643.229
Model 10	3480586.455 ± 669467.413	6846223.738 ± 2223237.831	22937902.126 ± 5540543.868

Table 2: Metrics Test Results for Ensemble and Individual Models (part 2)

RISb	CAM	Grad-CAM	Random
Ensemble	13.977 ± 1.240	14.575 ± 0.992	53.456 ± 1.641
Model 1	18.565 ± 1.301	18.565 ± 1.301	59.152 ± 1.826
Model 2	12.941 ± 0.917	12.970 ± 0.924	60.379 ± 2.114
Model 3	14.947 ± 0.944	14.909 ± 0.943	59.725 ± 1.783
Model 4	12.904 ± 0.687	13.256 ± 1.360	61.108 ± 1.750
Model 5	11.153 ± 1.096	11.154 ± 1.096	60.242 ± 1.856
Model 6	12.638 ± 1.369	12.698 ± 1.366	60.179 ± 2.090
Model 7	12.220 ± 0.823	12.921 ± 1.298	61.857 ± 1.852
Model 8	18.619 ± 0.839	18.606 ± 0.841	58.860 ± 2.132
Model 9	13.195 ± 0.815	9.910 ± 1.501	59.681 ± 1.949
Model 10	13.266 ± 1.256	19.019 ± 1.077	59.780 ± 1.875
ROS	CAM	Grad-CAM	Random
Ensemble	26378.525 ± 22364.341	41400.726 ± 40902.013	100282.533 ± 45148.804
Model 1	12358.423 ± 5107.679	12358.425 ± 5107.678	167488.094 ± 188907.518
Model 2	48508.845 ± 46128.105	48507.195 ± 46128.132	238020.249 ± 149941.173
Model 3	689995.736 ± 563561.376	688867.883 ± 563590.546	17526781.455 ± 24820904.705
Model 4	625495.413 ± 539095.851	616604.749 ± 730402.984	5222686.783 ± 4820274.414
Model 5	4888.137 ± 2348.803	4888.130 ± 2348.801	188705.842 ± 96210.421
Model 6	18761.681 ± 16394.279	11717.707 ± 7851.360	88558.495 ± 38702.627
Model 7	30960887.120 ± 49570977.534	2465358.603 ± 1545351.239	68234634.236 ± 65663999.020
Model 8	11131.461 ± 9793.839	11131.035 ± 9793.876	31365.712 ± 39137.823
Model 9	75462.505 ± 51427.097	30556.754 ± 23305.412	272482.338 ± 174124.522
Model 10	18182708708.536 ± 34033740331.051	3903058531927.605 ± 7702513374782.742	78180252904.944 ± 138655149933.328
RRS	CAM	Grad-CAM	Random
Ensemble	22.482 ± 2.343	24.196 ± 1.870	99.062 ± 6.989
Model 1	0.577 ± 0.290	0.577 ± 0.290	1.661 ± 0.726
Model 2	0.189 ± 0.138	0.189 ± 0.138	0.619 ± 0.478
Model 3	0.484 ± 0.300	0.484 ± 0.300	1.382 ± 0.708
Model 4	0.168 ± 0.117	0.198 ± 0.205	0.985 ± 0.547
Model 5	0.443 ± 0.252	0.443 ± 0.252	1.356 ± 0.729
Model 6	0.364 ± 0.242	0.417 ± 0.270	1.460 ± 0.753
Model 7	0.198 ± 0.165	0.236 ± 0.198	0.627 ± 0.479
Model 8	0.984 ± 0.401	0.984 ± 0.401	2.196 ± 0.879
Model 9	0.506 ± 0.241	0.268 ± 0.183	1.570 ± 0.747
Model 10	0.229 ± 0.199	0.347 ± 0.263	0.819 ± 0.581

Table 3: The architectures of the 10 models in the ensemble. Abbreviations: br., branch; bottl., bottleneck; MBC., mobile inverted bottleneck convolution; den., dense; mod., module; tmp., temporal; lin., linear; gl., global; sp., spatial; DA, disentangled aggregation; SC, spatial configuration; SE, Squeeze-and-Excitation; abs., absolute; ch., channel; ReLU, rectified linear unit; sw., swish; AUC, area under the receiver operating characteristic curve.

Architectural choice	1	2	3	4	5	6	7	8	9	10
No. modules of input br.	3	3	2	2	2	2	3	3	2	2
Width of input br.	10	10	12	10	8	6	8	6	12	12
Block type in initial mod.	Bottl.	Basic	Basic	Basic	Bottl.	Basic	Basic	MBC.	Bottl.	Basic
Residual type in initial mod.	None	Den.	None	Block	Den.	Den.	Mod.	Block	Den.	Den.
No. tmp. scales in input br.	1	3	2	2	3	2	2	1	2	2
No. levels of main br.	3	1	3	2	2	2	2	2	2	1
No. modules of main br. levels	3	2	1	1	3	3	2	3	1	1
Width of first level of main br.	12	12	12	10	12	12	10	12	8	12
No. tmp. scales in main br.	1	2	2	3	2	1	2	1	1	1
Pooling layer type	Gl.	Gl.	Gl.	Sp.	Sp.	Gl.	Gl.	Gl.	Gl.	Sp.
Graph convolution type	DA	DA	SC	DA	SC	DA	DA	DA	DA	SC
	2	4+2		4		4	2	2	4	
Block type	Basic	MBC.	Basic	Basic	Bottl.	Bottl.	Basic	Basic	Bottl.	Basic
Bottl. factor	4	2	2	2	2	2	4	4	4	4
Residual type	None	Block	Den.	None	None	Block	None	Den.	Block	None
SE type	None	Outer	Inner	None	Outer	None	None	Outer	Outer	None
SE ratio	-	2	2	4	2	4	4	4	4	4
SE ratio type	-	Abs.	Abs.	Abs.	-	Abs.	-	Abs.	Abs.	-
Attention type	Ch.	-	-	-	Ch.	-	Ch.	-	Ch.	-
Nonlinearity type	ReLU	Sw.	ReLU	Sw.	Sw.	ReLU	ReLU	Sw.	ReLU	Sw.
Tmp. kernel size	9	7	9	7	9	7	9	7	9	7
AUC	0.949	0.942	0.938	0.943	0.937	0.956	0.953	0.953	0.932	0.947

Table 4: Unpaired t-test result: CAM versus Grad-CAM (part 1)

PGI		
	t-statistic	p-value
Ensemble	0.346594	0.728908
Model 1	-0.059377	0.952654
Model 2	0.402978	0.686979
Model 3	0.038596	0.969214
Model 4	2.602390	0.009280
Model 5	-0.316427	0.751690
Model 6	-0.382246	0.702292
Model 7	-0.592449	0.553572
Model 8	0.063267	0.949556
Model 9	-5.950216	2.832418e-09
Model 10	1.353371	0.175988
PGU		
	t-statistic	p-value
Ensemble	-1.908225	0.056412
Model 1	0.015310	0.987785
Model 2	0.092156	0.926577
Model 3	0.141020	0.887859
Model 4	-3.460206	0.000544
Model 5	-0.136616	0.891339
Model 6	-0.018139	0.985529
Model 7	2.238301	0.025240
Model 8	0.019318	0.984588
Model 9	6.835406	9.093938e-12
Model 10	-2.544099	0.010982
RISp		
	t-statistic	p-value
Ensemble	-0.437441	0.661808
Model 1	-0.000016	0.999988
Model 2	-0.024395	0.980538
Model 3	0.493987	0.621334
Model 4	-1.033182	0.301573
Model 5	-0.000004	0.999997
Model 6	-0.183744	0.854220
Model 7	-2.225563	0.026086
Model 8	-0.002316	0.998152
Model 9	15.424594	1.675449e-52
Model 10	-24.577841	3.367287e-127
RISv		
	t-statistic	p-value
Ensemble	-4.928563	8.507249e-07
Model 1	-0.000004	0.999996
Model 2	-0.057351	0.954267
Model 3	0.025330	0.979793
Model 4	1.038284	0.299183
Model 5	0.000001	0.999999
Model 6	-0.372872	0.709257
Model 7	1.580504	0.114070
Model 8	0.023271	0.981435
Model 9	8.550714	1.555406e-17
Model 10	-8.233855	2.512258e-16

Table 5: Unpaired t-test result: CAM versus Grad-CAM (part 2)

RISb		
	t-statistic	
Ensemble	2.313236	0.020745
Model 1	-0.000016	0.999987
Model 2	-0.145161	0.884588
Model 3	0.167647	0.866867
Model 4	-1.296128	0.194995
Model 5	-0.000001	0.999999
Model 6	-0.105578	0.915920
Model 7	-3.081867	0.002068
Model 8	0.067254	0.946382
Model 9	12.590592	8.358464e-36
Model 10	-20.963022	3.321069e-94
ROS		
	t-statistic	p-value
Ensemble	0.852538	0.393952
Model 1	-0.000001	1.000000
Model 2	-0.000000	1.000000
Model 3	0.004623	0.996312
Model 4	0.053704	0.957173
Model 5	0.000005	0.999996
Model 6	0.883619	0.376956
Model 7	3.327644	0.000886
Model 8	0.000058	0.999954
Model 9	2.395027	0.016667
Model 10	-1.002149	0.316352
RRS		
	t-statistic	p-value
Ensemble	3.068542	0.002161
Model 1	-0.000000	1.000000
Model 2	-0.000000	1.000000
Model 3	-0.000000	1.000000
Model 4	-0.000000	1.000000
Model 5	0.000000	1.000000
Model 6	-1.152599	0.249122
Model 7	-0.914333	0.360580
Model 8	-0.000002	0.999998
Model 9	5.372476	8.077018e-08
Model 10	-2.785957	0.005355

Table 6: Unpaired t-test result: CAM versus Random Attribution (part 1)

PGI		
	t-statistic	p-value
Ensemble	3.228758	0.001250
Model 1	3.305932	0.000952
Model 2	4.870700	0.000001
Model 3	2.086048	0.037016
Model 4	4.119581	0.000038
Model 5	4.927732	0.000001
Model 6	2.081000	0.037476
Model 7	2.117884	0.034226
Model 8	4.061314	0.000049
Model 9	-0.138202	0.890085
Model 10	-1.668719	0.095226
PGU		
	t-statistic	p-value
Ensemble	-8.240703	0.000000
Model 1	-6.558054	0.000000
Model 2	-6.145350	0.000000
Model 3	-4.001890	0.000064
Model 4	-10.571248	0.000000
Model 5	-9.798438	0.000000
Model 6	-1.126884	0.259839
Model 7	-0.319122	0.749646
Model 8	-4.784537	0.000002
Model 9	1.025866	0.304999
Model 10	-1.681898	0.092643
RISp		
	t-statistic	p-value
Ensemble	-69.274966	0.000000
Model 1	-65.288282	0.000000
Model 2	-72.948463	0.000000
Model 3	-71.029458	0.000000
Model 4	-75.880358	0.000000
Model 5	-76.810741	0.000000
Model 6	-68.599757	0.000000
Model 7	-75.154906	0.000000
Model 8	-63.345906	0.000000
Model 9	-72.521749	0.000000
Model 10	-71.929170	0.000000
RISv		
	t-statistic	p-value
Ensemble	-24.344140	0.000000
Model 1	-20.114345	0.000000
Model 2	-24.965946	0.000000
Model 3	-21.361852	0.000000
Model 4	-23.671184	0.000000
Model 5	-26.727520	0.000000
Model 6	-20.797096	0.000000
Model 7	-24.131390	0.000000
Model 8	-21.404787	0.000000
Model 9	-19.301737	0.000000
Model 10	-24.397185	0.000000

Table 7: Unpaired t-test result: CAM versus Random Attribution (part 2)

RISb		
	t-statistic	p-value
Ensemble	-64.755147	0.000000
Model 1	-61.762571	0.000000
Model 2	-72.323794	0.000000
Model 3	-68.914145	0.000000
Model 4	-74.410386	0.000000
Model 5	-75.631103	0.000000
Model 6	-69.824165	0.000000
Model 7	-75.605835	0.000000
Model 8	-62.847825	0.000000
Model 9	-71.187557	0.000000
Model 10	-72.411265	0.000000
ROS		
	t-statistic	p-value
Ensemble	-3.342298	0.000836
Model 1	-1.645748	0.099920
Model 2	-3.598124	0.000325
Model 3	-2.312361	0.020826
Model 4	-2.644420	0.008225
Model 5	-4.820705	0.000001
Model 6	-4.349855	0.000014
Model 7	-1.872147	0.061255
Model 8	-1.033692	0.301357
Model 9	-3.696956	0.000221
Model 10	-1.496006	0.134750
RRS		
	t-statistic	p-value
Ensemble	-39.979699	0.000000
Model 1	-9.543686	0.000000
Model 2	-6.262358	0.000000
Model 3	-8.260879	0.000000
Model 4	-9.619116	0.000000
Model 5	-8.938158	0.000000
Model 6	-10.515924	0.000000
Model 7	-6.153502	0.000000
Model 8	-9.235283	0.000000
Model 9	-9.842633	0.000000
Model 10	-7.617952	0.000000

Table 8: Unpaired t-test result: Grad-CAM versus Random Attribution (part 1)

PGI		
	t-statistic	p-value
Ensemble	2.839915	0.004528
Model 1	3.369167	0.000759
Model 2	4.476108	0.000008
Model 3	2.046355	0.040764
Model 4	1.475531	0.140122
Model 5	5.247443	0.000000
Model 6	2.441880	0.014639
Model 7	2.781726	0.005424
Model 8	3.995221	0.000065
Model 9	5.820300	0.000000
Model 10	-2.938911	0.003307
PGU		
	t-statistic	p-value
Ensemble	-6.411041	0.000000
Model 1	-6.572715	0.000000
Model 2	-6.228821	0.000000
Model 3	-4.133470	0.000036
Model 4	-7.212538	0.000000
Model 5	-9.669277	0.000000
Model 6	-1.105639	0.268929
Model 7	-2.531826	0.011374
Model 8	-4.802966	0.000002
Model 9	-6.146440	0.000000
Model 10	0.920952	0.357114
RISp		
	t-statistic	p-value
Ensemble	-67.438628	0.000000
Model 1	-65.288262	0.000000
Model 2	-72.931395	0.000000
Model 3	-71.205931	0.000000
Model 4	-73.143467	0.000000
Model 5	-76.810740	0.000000
Model 6	-68.494628	0.000000
Model 7	-72.465331	0.000000
Model 8	-63.339157	0.000000
Model 9	-76.109905	0.000000
Model 10	-61.907950	0.000000
RISv		
	t-statistic	p-value
Ensemble	-23.174673	0.000000
Model 1	-20.114344	0.000000
Model 2	-24.940226	0.000000
Model 3	-21.366473	0.000000
Model 4	-23.743872	0.000000
Model 5	-26.727520	0.000000
Model 6	-20.680862	0.000000
Model 7	-23.590898	0.000000
Model 8	-21.412311	0.000000
Model 9	-22.667079	0.000000
Model 10	-18.506366	0.000000

Table 9: Unpaired t-test result: Grad-CAM versus Random Attribution (part 2)

RISb		
	t-statistic	p-value
Ensemble	-64.493624	0.000000
Model 1	-61.762544	0.000000
Model 2	-72.267119	0.000000
Model 3	-68.972703	0.000000
Model 4	-71.595163	0.000000
Model 5	-75.631103	0.000000
Model 6	-69.794548	0.000000
Model 7	-72.959298	0.000000
Model 8	-62.863070	0.000000
Model 9	-73.555998	0.000000
Model 10	-64.343782	0.000000
ROS		
	t-statistic	p-value
Ensemble	-4.421883	0.000010
Model 1	-1.645748	0.099920
Model 2	-3.598124	0.000325
Model 3	-2.312506	0.020818
Model 4	-2.653743	0.008002
Model 5	-4.820706	0.000002
Model 6	-5.196932	0.000000
Model 7	-3.603603	0.000319
Model 8	-1.033712	0.301347
Model 9	-4.809240	0.000002
Model 10	0.979096	0.327611
RRS		
	t-statistic	p-value
Ensemble	-40.463858	0.000000
Model 1	-9.543686	0.000000
Model 2	-6.262358	0.000000
Model 3	-8.260879	0.000000
Model 4	-9.029468	0.000000
Model 5	-8.938158	0.000000
Model 6	-9.841412	0.000000
Model 7	-5.519696	0.000000
Model 8	-9.235282	0.000000
Model 9	-12.332399	0.000000
Model 10	-5.896142	0.000000